https://doi.org/10.5194/egusphere-2026-2787
Preprint. Discussion started: 11 June 2026

Large-scale circulation and stratocumulus variability

Hairu Ding[1], Bjorn Stevens[1], Frank Lunkeit[2], and Nedjeljka Žagar[2]

[1]Max Planck Institute for Meteorology, Hamburg, Germany
[2]Meteorological Institute, Universität Hamburg, Hamburg, Germany

Correspondence: Hairu Ding (hairu.ding@mpimet.mpg.de)

Abstract. This study aims to understand the relationship between large-scale circulation and stratocumulus variability. We use reanalysis and satellite data to identify circulation patterns that couple with estimated inversion strength (EIS) and low-cloud cover (LCC) in stratocumulus areas. The results update the current understanding in two aspects: the limited direct influence of the tropical thermodynamic framework on stratocumulus, and the different responses of EIS and LCC to large-scale circulation.

Extratropical dynamics control EIS variability. From synoptic to interseasonal timescales (after deseasonalization), synoptic-scale Rossby ridges located directly over stratocumulus enhance stability throughout the tropospheric column and thereby increase EIS. On interannual timescales, planetary-scale Rossby waves coupled with a negative PDO-like (Pacific Decadal Oscillation-like) sea surface temperature pattern increase EIS. In contrast, LCC responds to circulation patterns similar to those associated with EIS, but with a systematic upstream (west and poleward) shift. This shift suggests a direct response of LCC to circulation through enhanced pressure gradients, which increase cold advection and offset the drying effect of Rossby ridges via stronger winds. The upstream Rossby ridges associated with increased LCC often overlap with the subtropical highs, which has led to the previous emphasis on thermodynamic processes that strengthen subtropical highs by enhancing the descending branch of the Hadley cell.

1 Introduction

Subtropical stratocumulus (Sc) play an important role in reflecting Earth's incoming solar radiation (e.g., Hartmann et al., 1992; Stephens, 2005; Wood, 2012). Understanding the mechanisms that control its variability is therefore essential for understanding the global energy budget. Sc, lying within the well-mixed boundary layer, are hypothesized to be controlled by lower-tropospheric stability (quantified by estimated inversion strength in this study, EIS). Stronger lower-tropospheric stability can suppress entrainment drying and favor more Sc (Stevens et al., 2001). Previous studies supported that hypothesis by a strong correlation between lower-tropospheric stability and Sc (quantified by low-cloud cover, LCC) on the annual cycle and interannual timescales (Klein and Hartmann, 1993; Wood and Bretherton, 2006). However, later studies with contradict results renew the discussion over the causality underlying this strong correlation. Myers and Norris (2013) found that EIS dominates the climatological variability in Sc, whereas Bretherton and Blossey (2014) suggested that EIS is less important for Sc changes in a warming climate. On shorter (synoptic and subseasonal) timescales, the correlation between lower-tropospheric stability and Sc also becomes weak. Klein (1997) found that no single factor can well represent the short-term variability in Sc.

Klein et al. (1995), who observed a covariance between Sc and conditions from the preceding day near the subtropical highs, suggested that short-term variability in Sc corresponds to the strength of the subtropical highs.

Regarding the large-scale mechanism, early works proposed a tropical thermodynamic framework that linked Sc variability to the subsidence branch of the Hadley cell (e.g., Klein and Hartmann, 1993; Schubert et al., 1995; Siebesma et al., 2004). This however doesn't explain the regional maximum of subtropical highs over the eastern ocean basins. The regional maximum is instead thought to result from interactions between the zonal-mean flow and orography in winter, and from thermally induced extra subsidence in summer (known as monsoon–desert mechanism; Rodwell and Hoskins, 1996, 2001). The monsoon–desert mechanism states how off-equator convection warms the upper troposphere and induces a Rossby wave train toward the subtropical Sc area. They also discussed how that convection influences regions to the east through Kelvin waves and extends this mechanism to the whole globe. Later studies examining the influence of the monsoon–desert mechanism implicitly showed the uncertainty in regional responses (Gaetani et al., 2011; Zhang et al., 2022; Chen et al., 2022, 2001; Cherchi et al., 2014; Zilli and Hart, 2021). In addition, Garfinkel et al. (2021) suggested that the method of Rodwell and Hoskins (1996), which fixes diabatic forcing to mimic monsoons, underestimates the nonlinearity of summer stationary waves. Nigam and Chan (2009) proposed that the influence of monsoons on subtropical highs is a secondary effect compared to the absence of winter storm tracks. As the effects of monsoons on subtropical highs remain debated, their influence on Sc is even more unclear.

Above discussion highlights the uncertain role of EIS and the tropical thermodynamic framework in influencing Sc variability. Furthermore, there are several questions remain. For instance, why does the correlation between EIS and LCC exhibit a dependence on timescale (1st paragraph)? If the timescale of cloud-mass adjustments is on the order of a week (Dong et al., 2001), why does Sc respond to conditions one day earlier (Klein et al., 1995), rather than to conditions further upstream? If the one-day-lagged covariance indicates an effect of subtropical highs on Sc variability, why is this covariance observed only on short timescales, but not on long timescales (Ding et al., 2025)?

This study aims to identify the large-scale mechanisms underlying Sc variability and to explain the above questions. The coupling between the LCC or EIS index time series and circulation variability is quantified through regression in global three-dimensional wave space. The spherical framework and the distinction between mid-latitude Rossby, inertia-gravity waves and equatorial waves provide a scale-dependent perspective on the dynamics underlying Sc variability. This study shows an important role of the extratropical Rossby wave dynamics, which can directly influence Sc. Details of data and wave-space analysis method are provided in §4. In the temporal domain, we decompose variability in synoptic, subseasonal, interseasonal and interannual timescales. The regression analysis is complemented by composite analysis; composites of high-EIS and high-LCC cases illustrate the different responses of EIS and LCC to similar large-scale circulation patterns (§5).

2 Data and Methods

2.1 Data

This study uses satellite observations for low-cloud cover (LCC) and ERA5 (the fifth generation European Centre for Medium-Range Weather Forecasts atmospheric reanalyses; Hersbach et al., 2017) for other quantities. Daily mean data in the period

1987-01-01–2019-12-31 is used to investigate synoptic, subseasonal, and interseasonal variations; monthly mean data in the same period is used for analyzing interannual variations.

Satellite observations of cloud cover are taken from CLARA-A3 (the third edition of the Satellite Application Facility on Climate Monitoring's cloud, albedo, and surface radiation dataset from advanced very-high-resolution radiometer data) product by EUMETSAT (European Organization for the Exploitation of Meteorological Satellites; Karlsson et al., 2022). CLARA-A3 data is provided on a 0.25° × 0.25° spatial resolution and has long records (42 years), which benefits climate studies. It provides separate fractions for low-, mid-, and high-clouds, and we take the low-clouds fraction to quantify LCC.

ERA5 are obtained from DKRZ (Deutsche Klimarechenzentrum) data pool. It is in 0.225° × 0.225° horizontal resolution and 37 pressure levels. The regression analysis applies F128 Gaussian grids (512×256 points along latitude and longitude lines). Basic variables such as winds, geopotential height, sea surface temperature (SST), atmospheric temperature, sea level pressure (SLP), and surface latent heat flux (LHF) are directly read from ERA5. The other factors, such as relative vorticity, divergence, and potential temperature, are diagnosed by the MetPy Python package (version 1.7.0).

2.2 Estimated inversion strength

EIS is diagnosed following Wood and Bretherton (2006):

$$\mathrm{EIS} = \mathrm{LTS} - \mathit{\Gamma}_{\mathrm{m}}\left(Z_{700} - \mathrm{LCL}\right) \tag{1}$$

where $\mathrm{LTS} = \theta_{700} - \theta_{1000}$ is the potential temperature difference between 700 and 1000 hPa, $\mathit{\Gamma}_{\mathrm{m}}$ denotes the moist lapse rate at the average temperature of 700 and 1000 hPa. Z denotes the geopotential height at 700 hPa. LCL is the lifting condensation level, which is fixed to be 500 m in the calculation. This height is assumed based on a 80% surface relative humidity (RH), which is also what Wood and Bretherton (2006) does, and then it is calculated by $\mathrm{LCL} \approx 125(T - T_{\mathrm{d}})$ where $(T - T_{\mathrm{d}}) \approx (100\% - \mathrm{RH})/5$ following the approximation suggested by Lawrence (2005).

In this study, we use EIS to describe lower-tropospheric stability. Some studies also simply use LTS to describe that. The differences between LTS and EIS in their association with LCC are smaller than the data source difference (Cutler et al., 2022; Park and Shin, 2019), which indicates that the difference between EIS and LTS are not important for the more tropical/subtropical regimes. Hence, we do not emphasize the distinction between the two indices.

2.3 Timescale decomposition

For variability within a year, we remove the annual cycle by subtracting daily climatology. The deseasonalized series are then decomposed into synoptic (< 15 days), subseasonal (15–90 days), and interseasonal (90–365 days) components. The synoptic component is derived by removing a 15-day running mean from the deseasonalized series. The subseasonal component is obtained using a band-pass filter defined as the difference between 90-day and 15-day running means. The interseasonal component is similarly obtained as the difference between the 365-day and 90-day running means. For interannual variability (> 1 year), we take a 12-month running mean of the monthly time series. Deseasonalization is not applied on the interannual series, as the 12-month running mean effectively removes the annual cycle.

https://doi.org/10.5194/egusphere-2026-2787
Preprint. Discussion started: 11 June 2026

2.4 Wave-space regression between regional LCC/EIS and global circulation

We study coupling between Sc and large-scale circulation by decomposing ERA5 data using the MODES software (Žagar et al., 2015). MODES performs a multivariate representation of the global circulation in terms of three-dimensional orthogonal vertical and horizontal structure functions — normal modes (i.e. eigenfunctions) of the linearized primitive equations. A single mode is defined by three indices: zonal wavenumber k, meridional mode index n and vertical mode index m. For every n, there are three wave solutions: Rossby waves describing geostrophically-balanced circulation on the sphere, and eastward-propagating and westward-propagating inertia-gravity (IG) waves solutions (EIG and WIG, respectively). Two special solutions, equatorially-trapped Kelvin and mixed Rossby–gravity (MRG) waves are included as the lowest or $n = 0$ EIG and Rossby wave, respectively. The modal solutions for the zonal mean state ($k = 0$) follow Kasahara (1976). Our setup applies 200 zonal wavenumber, 19 vertical modes and 70 meridional modes for every wave types making a total of 210 meridional modes.

Vorticity-dominated MRG waves (Neduhal et al., 2024) and Rossby waves are collectively referred to as Rossby modes, and WIG and EIG modes including Kelvin wave are collectively referred to as IG modes. The tropical trapped MRG and Kelvin modes are included in the analysis because Sc areas are located in the subtropics and we also consider interannual timescales. Geostrophically balanced Rossby waves on the sphere have a small divergence associated with the β term, proportional to $v_g\beta/f$, where v_g is the meridional geostrophic wind. The isallobaric motions, i.e. most of ageostrophic dynamics related to the baroclinic Rossby wave dynamics, projects on the IG modes. This means that mid-latitude IG modes are a mixture of ageostrophic circulation, internal IG and gravity waves due to various sources and some coherent structure across scales that are not waves (see discussion in Žagar et al., 2023).

At each time step with data, modal decomposition produces a dimensionless expansion coefficient $\chi_n^k(m)$. Applied step-by-step to daily/monthly ERA5 data, MODES provides time series $\chi_n^k(m,t)$ that can be correlated with time series of EIS or LCC indices, denoted $\mathcal{I}$. The lagged regressions between $\mathcal{I}$ and $\chi_n^k(m,t)$, $\mathcal{R}_n^k(m,\tau)$, is computed as:

$$\mathcal{R}_n^k(m,\tau) = \frac{1}{N-1}\frac{\sum_{t=1}^{N}[(\chi_n^k(m,t+\tau) - \overline{\chi_n^k(m)})(\mathcal{I}(t) - \overline{\mathcal{I}})]}{\mathrm{var}(\mathcal{I})}, \qquad (2)$$

where τ denotes the lag, N denotes the length of records, and var denotes temporal variance. The overbar in this equation denotes temporal mean.

We compute $\mathcal{R}_n^k(m,\tau)$ separately for $\mathcal{I}$ for each Sc area and for each of the time series isolating different timescales as described above. We also do the same regression for an open-ocean area in the subtropics in order to compare the near-field orographic effects. Indices t and τ are in days for the synoptic, subseasonal, and interseasonal series, and in months for the interannual series. The resulting complex variable $\mathcal{R}_n^k(m,\tau)$, a normalized covariance between circulation and Sc area index, can be projected back to physical space of 3D global wind and geopotential anomalies associated with variability represented by the index $\mathcal{I}$. Such filtering already identified circulation modes associated with the Madden-Julian Oscillation (MJO; Žagar and Franzke, 2015) and equatorial wave circulation coupled with a deep convection over the subtropical western North Pacific (Chen et al., 2025).

https://doi.org/10.5194/egusphere-2026-2787
Preprint. Discussion started: 11 June 2026

By limiting physical-space transformation of the complex vector $\mathcal{R}$ to elements associated with only Rossby or IG modes, we filter geopotential height (Z) and wind (u, v) perturbations associated with Rossby and IG waves, respectively. The IG-mode field filtered in this way is used to compute the vertical pressure velocity (ω) from the continuity equation, starting from the top level in the data ($125\,\mathrm{hPa}$).

The squared amplitude of the regression field, $gD_m|\mathcal{R}_n^k(m,\tau)|^2$, can be integrated along any dimension (k, n, or m) to provide the normalized covariance as a function of the remaining dimensions; for example, $\sum_m \sum_n gD_m|\mathcal{R}_n^k(m,\tau)|^2$ provides the zonal wavenumber distribution of the covariance between the global circulation and the $\mathcal{I}$. The multiplication factor gD_m consists of the gravity g and the equivalent depth D_m associated with vertical mode m, and it returns dimension of energy per unit mas (J/kg) to the covariance (removed in the process of projection). The covariance spectrum can further be split between Rossby and IG modes to identify both scales and wave dynamics associated with the $\mathcal{I}$. Here we note that each Sc area is normalized by a different variance meaning that their variance spectra, as well as u, v and Z anomalies for different $\mathcal{I}$ and timescales are not comparable in terms of amplitudes.

2.5 Jet Identification

The identification of polar front jets and subtropical jets follows the method of Liu et al. (2021) and uses 1987–2019 climatology. Polar front jets are detected by the maximum in zonal winds at $850\,\mathrm{hPa}$, within 37°–65° N/S. Subtropical jets are detected by the maximum shear between 250 and $850\,\mathrm{hPa}$ within 10°–40° N/S. This method helps to separate polar front and subtropical jets based on the baroclinic structure of subtropical jets. Afterwards, we apply Gaussian smoothing with $\sigma = 5$ for visualization.

2.6 Wave activity flux

To diagnose energy propagation independent from wave phase, we compute the three-dimensional wave activity flux $\mathbf{F} = (F_\lambda, F_\varphi, F_p)$ following Takaya and Nakamura (2001), expressed in terms of wind components in pressure coordinates:

$$\begin{aligned}
F_\lambda &= \frac{p\cos\varphi}{2\|\bar{V}\|}\left[\bar{u}(u'^2 - v'^2) + 2\bar{v}u'v'\right] \\
F_\varphi &= \frac{p\cos\varphi}{2\|\bar{V}\|}\left[2\bar{u}u'v' + \bar{v}(v'^2 - u'^2)\right] \\
F_p &= -\frac{p\cos\varphi}{\|\bar{V}\|}\frac{f^2}{N^2}(\bar{u}u'\omega' + \bar{v}v'\omega')
\end{aligned} \tag{3}$$

where u, v, ω denote the zonal, meridional, and vertical velocity, respectively; p is pressure, φ is latitude, λ is longitude, and θ is potential temperature. The overbar denotes zonal mean, and the prime denotes deviation from zonal mean. $\|\bar{V}\| = \sqrt{\bar{u}^2 + \bar{v}^2}$ denotes zonal-mean wind speed, $f = 2\Omega\sin\varphi$ is the Coriolis parameter, and $N = \sqrt{(g/\bar{\theta})(\partial\bar{\theta}/\partial z)}$ is the Brunt–Väisälä frequency. Here g, Ω, a are the gravity, Earth's rotation rate, and Earth's radius, respectively. Negative F_p indicates upward wave energy propagation.

To avoid infinite values in the planetary boundary-layer, negative or near-zero values of N^2 were set to a very small value ($10^{-6}\,\mathrm{s}^{-2}$). This preserves the direction of vertical flux while stabilizing the numerical computation.

https://doi.org/10.5194/egusphere-2026-2787
Preprint. Discussion started: 11 June 2026

The fluxes $(F_\lambda, F_\varphi, F_p)$ were computed using daily data at each grid point, and they were saved as three-dimensional (p, φ, λ) arrays for subsequent composite analyses.

2.7 Near surface temperature advection

The near surface temperature advection (T_{adv}) is diagnosed by:

$$T_{\mathrm{adv}} = -\boldsymbol{v_{1000}} \cdot \nabla T_{1000} = -\left(\frac{u_{1000}}{a\cos\varphi}\frac{\partial T_{1000}}{\partial\lambda} + \frac{v_{1000}}{a}\frac{\partial T_{1000}}{\partial\varphi}\right) \tag{4}$$

using central finite difference. Here $\boldsymbol{v_{1000}}$ denotes the 1000 hPa horizontal wind vector, T_{1000} denotes 1000 hPa temperature.

2.8 Coherence

We use the SciPy Python package (version 1.14.1) to compute the coherence between two daily time series from 1987–2019. This package is based on Welch's method, in which the time series is divided into overlapping segments and the Fourier transform is applied to each segment independently. Given a total record length of 12053 days, we choose a window size of 3000 days. This window size provides sufficient frequency resolution for interannual signal shorter than 7 years. With this window size and a 50% overlap, the significance thresholds of coherence are approximately 0.4 and 0.32 at the 95% and 90% levels, respectively. For visualization, we remap the coherence onto a logarithmically spaced frequency axis using linear interpolation. A 3-point running mean is then applied to the logarithmically spaced coherence to smooth the plots.

3 Overview of LCC and EIS

The climatology of low-cloud cover (LCC) and estimated inversion strength (EIS) show similar distribution patterns (Figure 1 a–b). Five Sc areas (blue contours) are identified based on the climatological LCC exceeding 40% in the North Atlantic (NA) and 50% in other regions, including North Pacific (NP), South Indian Ocean (SI), South Pacific (SP), and South Atlantic (SA).

Beyond the spatial pattern, panel c of Figure 1 shows the coherence between LCC and EIS across timescales. Their coherence is strong on interseasonal (90–365 days) and interannual (> 365 days) timescales, with a peak at the annual cycle (around 365 days). The coherence on synoptic (< 15 days) and subseasonal (15–90 days) timescales is weaker and slowly increasing going from day-by-day to seasonal timescales.

The coherence between EIS and potential temperatures (θ) in panel d, provides insight into its controlling processes. It suggests that EIS is dominated by free-tropospheric processes on synoptic and subseasonal timescales, while the influence of θ_{1000} becomes important on longer timescales.

Based on c and d, we decompose the original daily series of EIS and LCC into four components: synoptic, subseasonal, interseasonal, and interannual (see method in §2.3). Even though there is no clear boundary between synoptic and subseasonal coherence, the 2-week timescale is typical for weather prediction as an initial-value problem and is associated with traveling, synoptic-scale baroclinic Rossby waves, whereas variability on subseasonal timescales is coupled to quasi-stationary, planetary-scale waves. The variance for each series of LCC after that decomposition is shown in Table 1. Synoptic and sub-

https://doi.org/10.5194/egusphere-2026-2787
Preprint. Discussion started: 11 June 2026

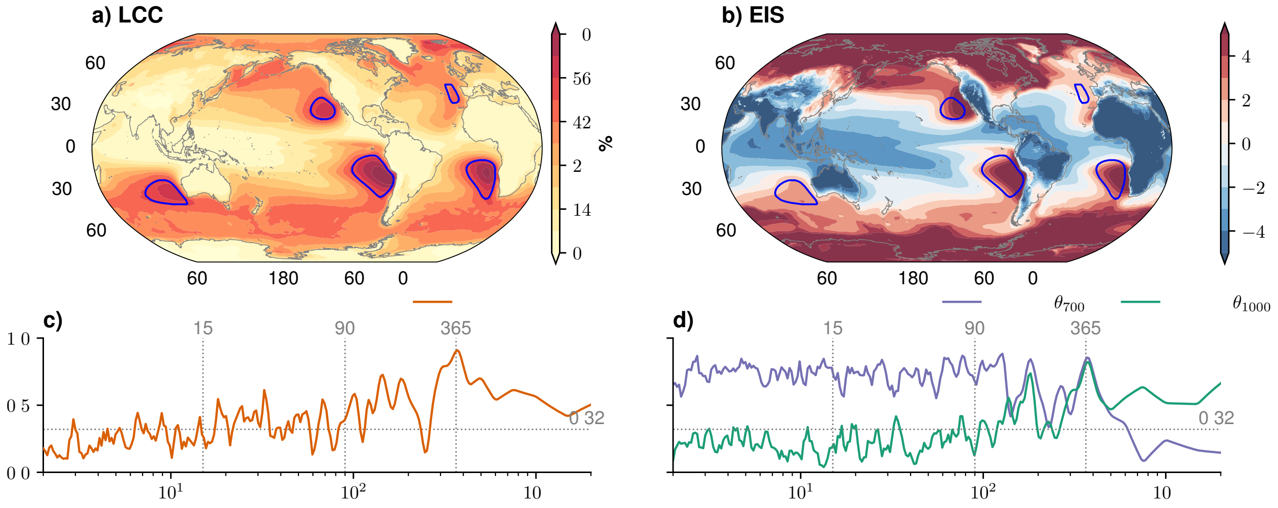

Figure 1. LCC (a) and EIS (b). Blue contours mark Sc areas (climatological LCC exceeding 40% in the North Atlantic (NA) and 50% in other regions). c) coherence of LCC versus EIS across timescales. d) coherence of EIS versus θ_{700} and θ_{1000} across timescales. c–d) use the mean time series over the five Sc areas. It represents the common features across Sc areas (Figure S1 in the Supplement). Coherence exceeding 0.32 are significant at the 90% level. The computation and smoothing method for coherence is introduced in §2.8.

seasonal variability accounts for the major part of LCC variability. To note, as we use running mean to perform timescale decomposition, the values are approximate variances for each timescale. We also quantified variances on each timescale through
185 the Fourier series decomposition (Table S1). It also shows that synoptic and subseasonal variability account for the majority of LCC variability, while the subseasonal variances are more comparable to that of synoptic timescales.

Table 1. Variance of LCC (unit: %) for each time series. The subscription 'orig' denotes the original daily series; 'deseas' denotes the series removing daily climatology; 'synoptic', 'subseasonal', 'interseasonal', and 'interannual' denote the respective series introduced in §2.3.

	σ^2_{orig}	$\sigma^2_{\mathrm{deseas}}$	$\sigma^2_{\mathrm{synoptic}}$	$\sigma^2_{\mathrm{subseasonal}}$	$\sigma^2_{\mathrm{interseasonal}}$	$\sigma^2_{\mathrm{interannual}}$
NP	492	331	192	76	18	15
NA	501	461	272	106	27	11
SI	279	252	165	50	14	8
SP	221	120	66	25	10	7
SA	247	150	91	30	9	7

4 Circulation controlling EIS and LCC on different timescales

This section shows the identified circulations controlling EIS and LCC for each Sc area (see the method in §2.4).

Figure 2 shows the zonal wavenumbers spectra of the normalized circulation covariance associated with LCC. Synoptic-scale ($k = 4$–8) waves play the dominant role on synoptic timescales in all seasons and regions. These synoptic-scale waves remain important on longer timescales (subseasonal and interseasonal) and still pronounce as a secondary peak on interannual timescales, while planetary-scale ($k = 1$–3) waves become increasingly important toward longer timescales.

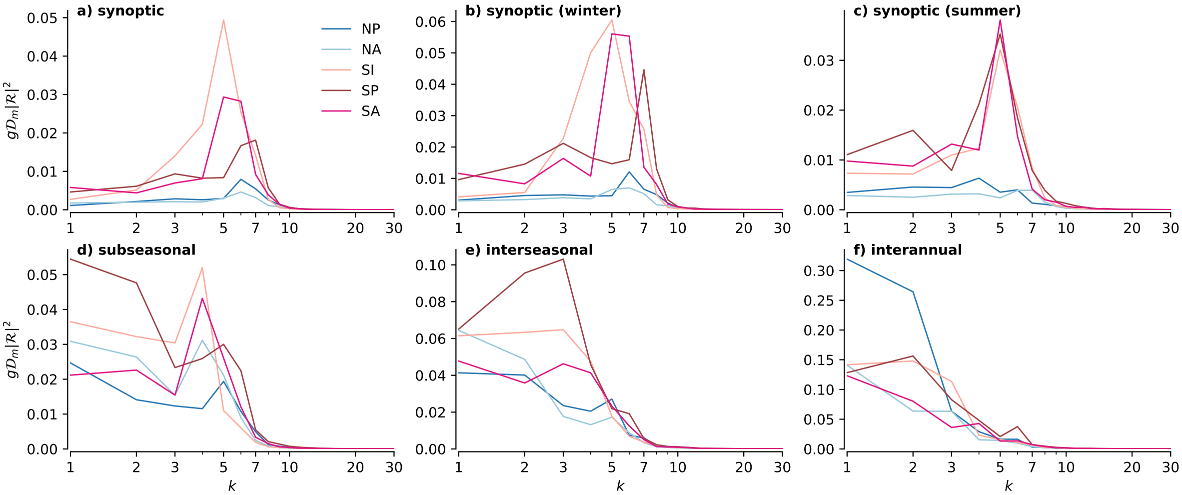

Figure 2. Zonal wavenumber (k) distribution of the covariance between global circulation and LCC for Rossby modes, with each region represented by a different color. See §2.4 for details of the method. (Version for EIS in Figure S2.)

4.1 Synoptic timescales

Figure 3 shows synoptic-timescale Rossby-mode geopotential height perturbations. Each row represents one region. We see that the circulation controlling synoptic EIS and LCC variability is an extratropical Rossby wave, with spatial scales reflecting Fig. 2a. An important difference between EIS and LCC is that the LCC-related Rossby wave (contour lines) is somewhat shifted upstream relative to that associated with EIS (filled contours). This location shift indicates that peak LCC variability preferentially occurs in the upstream Rossby wave ridge position, rather than collocated with it. We will return to the reason for this upstream preference in §5.2.

A synoptic-scale Rossby wave from upstream (west and poleward) originates several days ahead and propagates energy downstream. The zonal scale of this wave is equivalent to $k = 5$ wave (Figure 2a). The signal is localized, as the $k = 5$ Rossby waves are rarely circumglobal. On day 0, a Rossby ridge around Sc areas influences EIS and LCC. This ridge is associated with anticyclonic-wind perturbation (not shown). The vertical cross-sections indicate that this Rossby wave is almost barotropic but has a maximal amplitude in the upper troposphere. Later in §5.1, we discuss how this Rossby ridge increases EIS.

205 Behaviors of the synoptic-scale Rossby wave are influenced by both jets and orography. The subtropical jets (solid thick line) and the polar front jets (dashed thick line) act as waveguides for the synoptic-scale Rossby wave (Polster and Wirth, 2023). Rossby waves on the sphere tend to propagate equatorward unless stopped by jets (Hoskins and Karoly, 1981; Hoskins and Ambrizzi, 1993; Wirth, 2020). Due to the waveguide, synoptic-scale Rossby waves cannot fully reach the Sc areas that are closed to the equator (i.e., SP and SA). Therefore, SP and SA show smaller synoptic variability (Table 1), as they are less 210 perturbed.

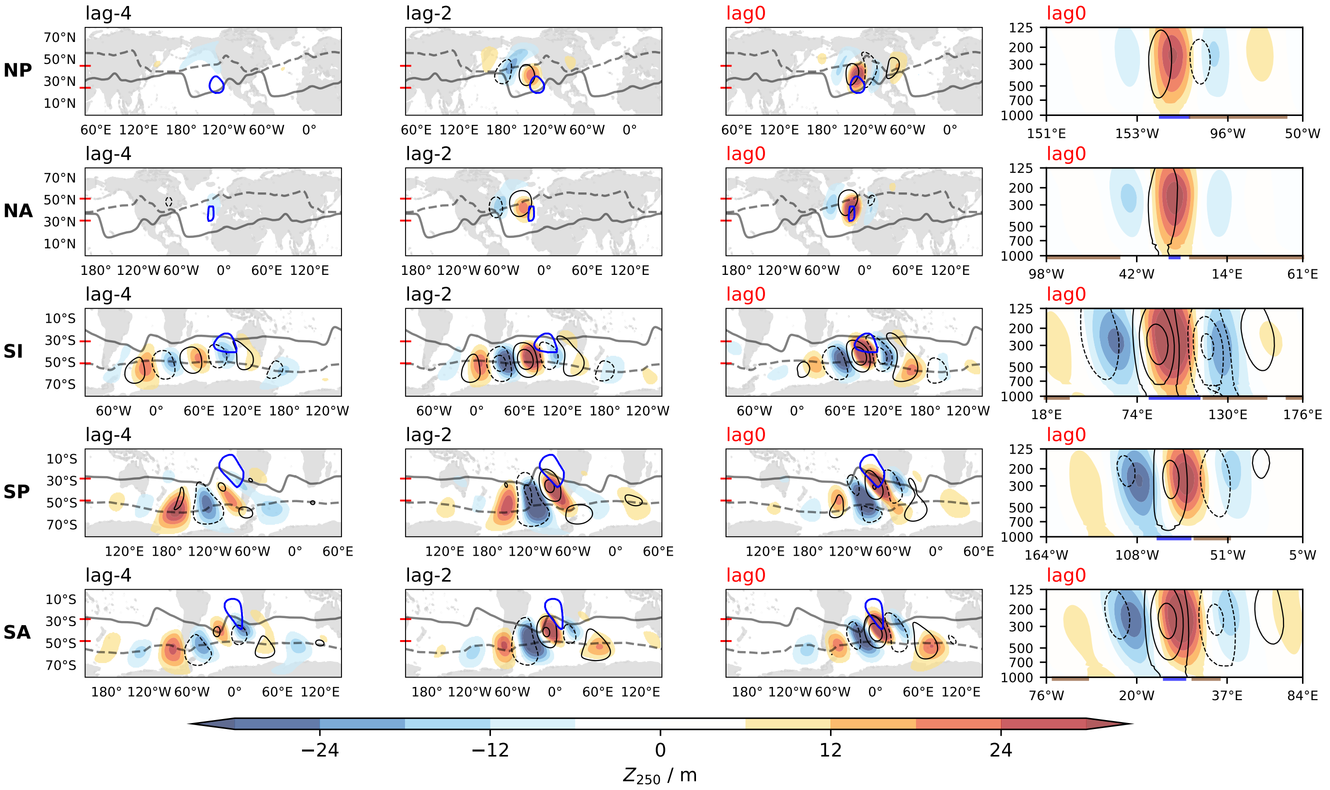

Figure 3. Geopotential height (Z) perturbation in Rossby modes associated with EIS (filled contours) and LCC (contour lines) on synoptic timescales. Maps show Z at 250 hPa. The thick gray solid line marks subtropical jets, and the thick dash line marks polar front jets. The blue contour marks the Sc area. Each row represents one region. 'lag-4' denotes circulation leads EIS/LCC by 4 days. The right column shows the cross-section averaged between latitudes marked by the red ticks on the map. The thick blue and brown underlines of the cross-section represent Sc areas and continents, respectively. (Winter and summer versions in Figures S7–8.)

Vertical velocity perturbations are due to IG modes (Žagar et al., 2023). The vertical velocity patterns in Fig. 4 are roughly in quadrature with the Rossby modes geopotential height (Figure 3). The quadrature relationship between Rossby wave geopotential and vertical velocity is consistent with quasi-geostrophic theory; air subsides in the negative vorticity advection region rather than at the center of highs. Neduhal et al. (2024) showed that the quadrature relationship holds for any linear wave

https://doi.org/10.5194/egusphere-2026-2787
Preprint. Discussion started: 11 June 2026

215 solutions. We don't observe other source of vertical velocity perturbations that could originate from tropical convections such as monsoons. This result suggests that the direct effect of monsoon on Sc is negligible compared to that of extratropical Rossby waves, in agreement with the similar arguments by Nigam and Chan (2009) for anticyclones in the subtropics.

The quadrature relationship between Rossby and IG modes remains on all timescales (Figures 3–6). Due to this quadrature relationship, the subsidence perturbations caused by Rossby ridges locate on the east edge of Sc. The compensate ascending 220 motions locate on the west edge (cross-sections in Figure 4, compare the dipole of color with the blue underline). This setup makes subsidence averaged over the Sc area a poor predictor for EIS variability, which explains EIS appears to be independent from subsidence in the same area (Myers and Norris, 2013; Ding et al., 2025).

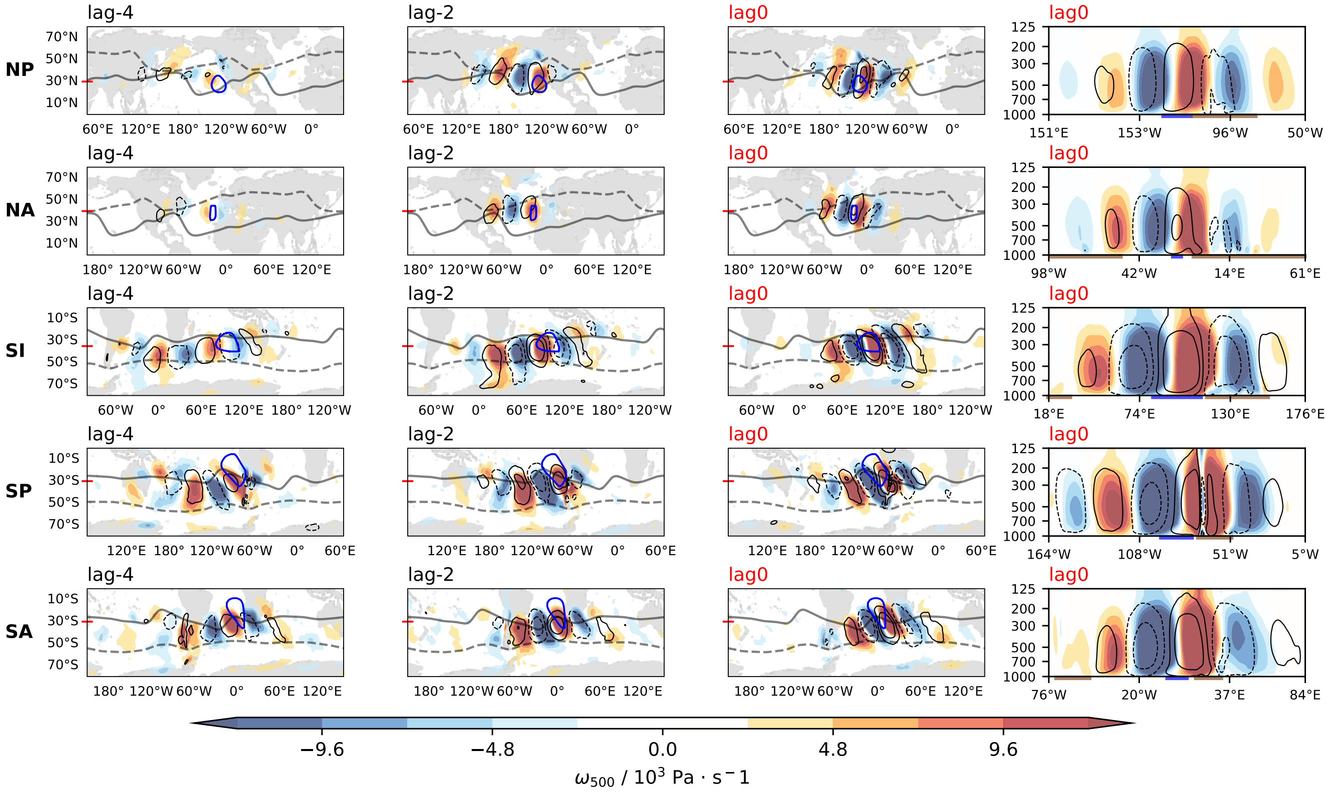

Figure 4. Vertical velocity (ω) perturbation in IG modes associated with EIS (filled contours) and LCC (contour lines) on synoptic timescales. Maps show ω at 500 hPa. The blue contour marks the Sc area. Each row represents one region. 'lag-4' denotes circulation leads EIS/LCC by 4 days. The right column shows the cross-section along the latitude marked by the red tick on the map. The thick blue and brown lines at the bottom of cross-sections represent Sc areas and continents, respectively. (Winter and summer versions in Figures S9–10.)

https://doi.org/10.5194/egusphere-2026-2787
Preprint. Discussion started: 11 June 2026

4.2 Subseasonal and interseasonal timescales

Figure 5 shows circulation controlling subseasonal variability in EIS and LCC (NP as the example). We see a combined pattern of a planetary-scale Rossby wave (around 60°N) and a localized synoptic-scale Rossby wave (around 20°–40°N). The localized synoptic-scale Rossby wave shows similar pattern to that of Figure 3, and the planetary-scale Rossby wave indicates the stationary wave in mean flow induced by Rocky Mountains (Charney and Eliassen, 1949). This orography-induced planetary-scale wave does not exhibit an obvious oscillation signal (compare lag-30 with lag0).

In contrast, the subseasonal variability of EIS/LCC over the open ocean is associated with an oscillation of the planetary-scale wave on a monthly timescale. This difference further supports the influence of near-field orographic forcing over the Sc area, which allows synoptic-scale Rossby waves to continue controlling Sc variability on subseasonal timescales. Other Sc areas with smaller orography, such as SI, show a similar dependence on the planetary-scale wave as the open ocean does. (Details in Figures S4 and S11.)

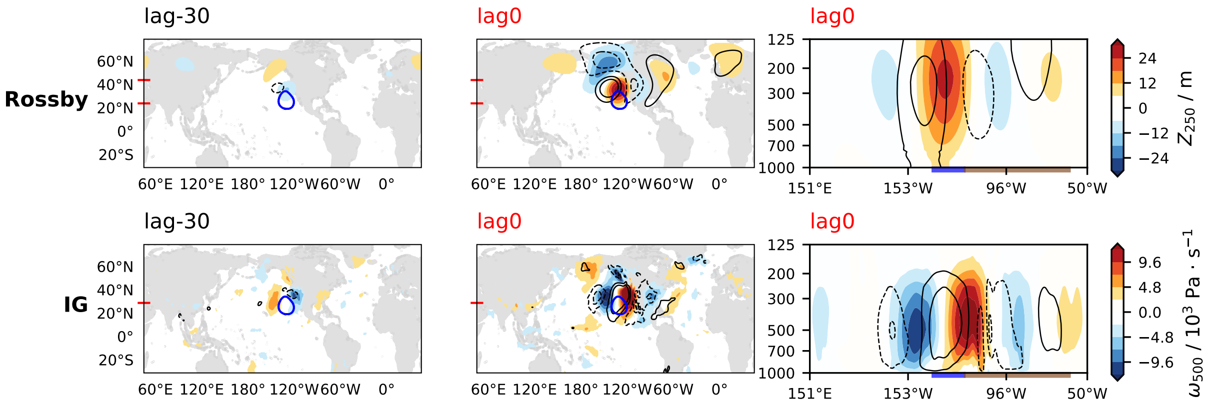

Figure 5. Geopotential height perturbation in Rossby modes (upper row) and vertical velocity perturbation in IG modes (lower row) associated with NP EIS (filled contours) and LCC (contour lines), respectively, on subseasonal timescales. The other visualization settings are similar to Figures 3 and 4. 'lag-30' indicates that the circulation leads EIS/LCC by 30 days. (Rossby modes for all regions are in Figure S10.)

The interseasonal results show circumglobal waves extending into the subtropics (with NA as an exception). These waves are not coupled with SST anomalies. It is worth noting that, because we removed the annual cycle, the circumglobal waves represent interseasonal oscillations apart from seasonality. Still, no signal of monsoon-induced perturbations is observed. In comparison, the interseasonal pattern over the open ocean exhibits a monsoon teleconnection when EIS there requires additional subsidence to increase. (Details in Figures S5 and S12.)

4.3 Interannual timescales

Figure 6 demonstrates coupling between EIS/LCC variability in NP and global circulation on interannual timescales. The IG-mode tropical pattern is similar to the perturbation in La Niña–like events with ascending (blues in the lower row) around the Maritime Continent and a descending (reds in the lower row) over the central–eastern equatorial Pacific, indicating an enhanced

Walker circulation. The compensating upper-level convergence associated with descending branch of this perturbation redistributes absolute vorticity and induces a Rossby wave source in the subtropics (Sardeshmukh and Hoskins, 1988). The induced
245 Rossby-mode circulation in the subtropics is $n = 1$ mode (blues in the upper row) with higher n associated with extratropical signals (patterns at higher latitudes in the upper row). This is a typical pattern associated with stationary response to large-scale tropical heating perturbations.

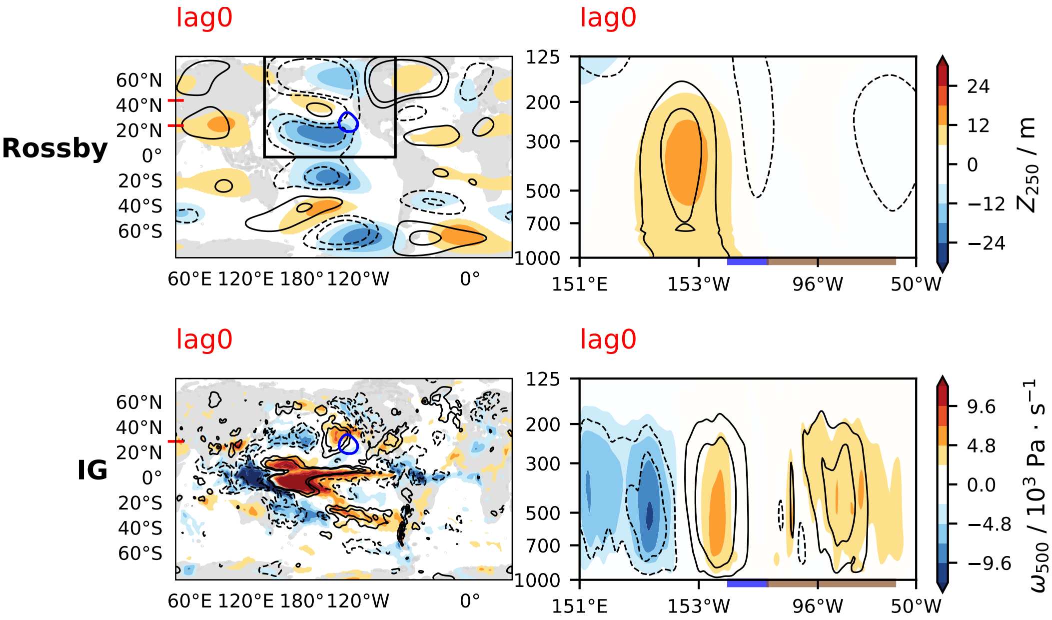

Figure 6. Geopotential height perturbation in Rossby modes (upper row) and vertical velocity perturbation in IG modes (lower row) associated with NP EIS (filled contours) and LCC (contour lines), respectively, on interannual timescales. The other visualization settings are similar to Figures 3 and 4. (Maps for all regions in Figure S14.)

Apart from tropical heating perturbations, a similar Rossby-mode pattern with a low–high–low meridional structure can also be associated with EIS/LCC variability when its subtropical signal is weak. These results suggest that the upstream high (reds in
250 the black box) has a more robust association with Sc, regardless of whether this structure is induced by extratropical or tropical perturbations, or by a combination of both. This upstream high is coupled with a localized SST pattern in the respective ocean basin: an upstream warm tongue with cooler SST in the Sc area. This coupling is indicated by the Rossby-mode cross-section in Figure 6. We refer to this atmosphere–ocean coupled pattern as the negative phase of a Pacific Decadal Oscillation–like (-PDO-like) pattern hereafter.

255 Hence, tropical perturbations are not the direct driver controlling the interannual variability of Sc. Instead, their influence is more likely nonlinear: they can induce a poleward Rossby wave train (first paragraph of §4.3) and influence the location of jets (Liu et al., 2021), thereby affecting the propagation of synoptic-scale Rossby waves (discussed in §4.1). In comparison, the -PDO-like pattern exerts a more direct influence on Sc (see further discussion in §5.3).

5 Composite results for high-EIS and high-LCC cases

In this section, we compare the common and distinct conditions for cases when EIS/LCC exceeds the 90th percentile. We call them the high-EIS and high-LCC cases, respectively.

5.1 Synoptic evolution

Figure 7 shows the evolution for high-EIS cases from six days prior (lag-6) to the reference day (lag0). When a Rossby ridge approaching Sc, the geopotential height anomaly keeps increasing there, and so does the θ_{700} (panels a and b). SST doesn't change much, supporting that Ekman pumping in the ocean has little influence on EIS. Meanwhile, θ_{1000} cools more than SST, indicating that the cooling is mainly due to the boundary-layer processes in the atmosphere.

Cross-sections in Figure 7 show geopotential height anomalies (Z', filled counters) under the synoptic-scale Rossby wave perturbation. The blue underline indicates the Sc area and the brown underlines indicate lands. The right brown underline in panels c–f represents North America. Arrows denote wave activity fluxes, which indicate the direction of energy propagation independent of wave phase (Takaya and Nakamura, 2001). We observe that wave energy mainly propagates from west to east. The propagation is stronger upstream of the Rocky Mountains. We observe wave activity convergence around the Sc area, as the eastward wave activity fluxes upstream meet the westward ones above the Rocky Mountains (arrows in panels c–f). This convergence is associated with an amplified high-pressure anomaly in the Sc area, which is similar to the orographic phase-locked amplification effect observed in Jiménez-Esteve et al. (2022). Jiménez-Esteve et al. (2022) show this amplification effect preferentially acts on k =5–6 waves, which are the dominant waves for Sc on the synoptic timescales (panels a–c of Figure 2).

On day 0, Z' shows a two-maxima structure: one near the surface and the other in the upper troposphere. Performing a similar analysis away from orography shows that the maximum in the upper troposphere vanishes, and thus the amplified high anomalies is speculated to due to the near-field orographic effects. The amplified high anomalies continuously warm θ_{700} for several days as a synoptic-scale Rossby ridge passes by (see panel b).

The two-maxima structure of Z' is associated with a positive θ' between $500\,\mathrm{hPa}$ and $850\,\mathrm{hPa}$, as well as a negative θ' within the boundary-layer (panel f and j). This distribution of Z' and θ' fits the hypsometric equation. θ' centered at the level of the largest gradient of Z'. However, the mechanism for the boundary-layer cooling is not that clear. We speculate this is due to the near-surface cold advection under the anticyclonic perturbation. The near-surface cold advection can create a cold-high anomaly in the boundary-layer, while the upper-level anticyclone warms the free troposphere. We don't know how much contribution of the surface latent heat flux and radiative cooling of clouds. Hotz et al. (2024) studies the 3D Lagrangian trajectory of the anticyclone over land, and they found the boundary-layer has a different thermal response to anticyclone compared to the free troposphere. Thus, we refer to the low-level baroclinic change of θ as the column response under synoptic-scale Rossby ridge perturbation. EIS is increased by this column response.

Panels k–n in Figure 7 show the evolution of SLP and $1000\,\mathrm{hPa}$ winds. A positive SLP anomaly locates over the Sc area on day 0, with winds circulating around it. This localized SLP anomaly is located downstream of subtropical highs, indicating that a localized increase in pressure is not necessarily caused by a strengthening of the subtropical highs, but instead results from the enhancement associated with a passing synoptic-scale Rossby ridge. This explains why EIS decorrelates from the strength of the subtropical highs (Ding et al., 2025).

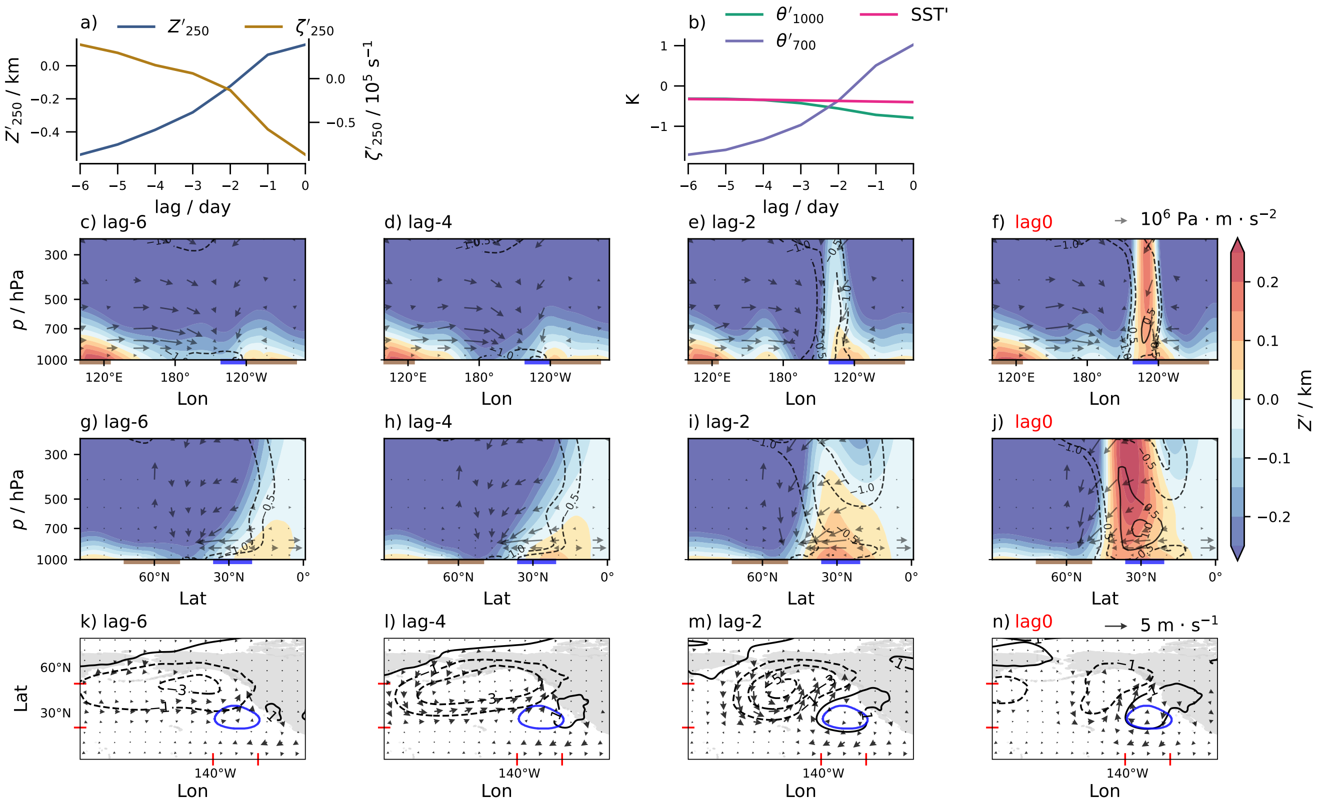

Figure 7. Synoptic evolution from lag-6 to lag0 days for composite high-EIS cases in NP. a) 250 hPa geopotential height (Z) and relative vorticity (ζ) anomaly. b) potential temperature (θ) and SST anomaly. Prime denotes anomaly. a–b) show values averaged over the Sc area (blue contour in k–n). c–f) zonal and g–j) meridional cross-sections of Z' (filled contours), θ' (contour lines, only visualize -1, -0.5, 0.5, and 1), and wave activity flux (arrows, the vertical direction is multiplied by 10^6 for visualization). The averaged latitude/longitude range used for the zonal/meridional cross-sections are marked by the red ticks in k–n. k–n) sea level pressure anomaly (unit:hPa, contour lines) and 1000 hPa winds anomaly (wind vectors).

5.2 Different responses of LCC and EIS to large-scale circulation

295 Here we discuss why LCC prefers a Rossby ridge that shifts about 10° upstream.

Figure 8 shows a similar mechanism to the high-EIS cases in Figure 7. However, LCC prefers a SLP anomaly that is centered upstream (panel f). This upstream SLP anomaly is aligned with the position of subtropical highs, explaining why studies observed the association between enhanced subtropical highs and larger LCC (Klein, 1997; George and Wood, 2010; Toniazzo et al., 2011). Averaging factors over a 10° upstream area (the blue box in Figure 8), the geopotential anomaly peaks about one day prior, consistent with Klein et al. (1995). This upstream high enhances the pressure gradient between upstream and the Sc area. The enhanced pressure gradient strengthens the near-surface winds along the Lagrangian trajectory of Sc.

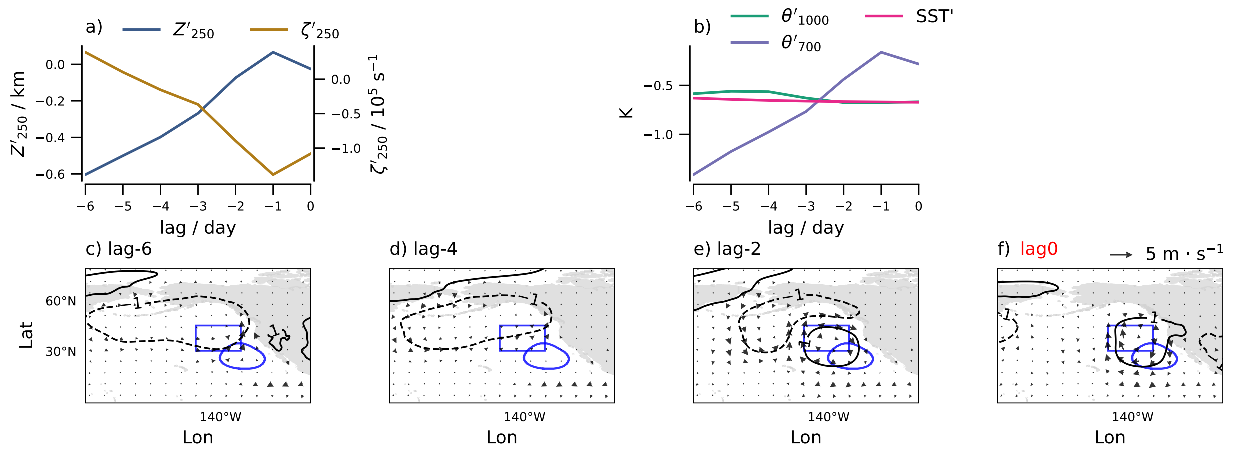

Figure 8. Similar to the 1st and 4th rows of Figure 7 but for composite high-LCC cases. a–b) show values averaged over the blue box in c–f) which is 10° west and poleward of the Sc area (blue contour).

Stronger near-surface winds can increase both near-surface cold advection ($-T_{\mathrm{adv}}$) and evaporation (represented by negative latent heat flux, -LHF). Figure 9 compares them between high-EIS and high-LCC cases. It shows that during the evolution of high-LCC cases (solid lines), cold advection is stronger (with approximately 40% larger range) and negative latent heat flux is larger (by approximately 80%) compared to high-EIS cases (dash lines). Cold advection can enhance mixing in the marine boundary-layer and increase Sc (Klein et al., 1995; Wood and Bretherton, 2004; Scott et al., 2020). Negative latent heat flux (i.e., evaporation) can serve more moisture. In the 3rd panel, we see how this moisture supply cancels the drying effect of the Rossby ridge coming from the west poleward. This canceling effect is more significant in the middle of the boundary-layer (e.g., 950 hPa). We don't observe a significant canceling effect at the 1000 hPa or 700 hPa level. Thus, taking into account moisture would be helpful to predict LCC, but which level to select may also influence how much it improves compared to solely considering EIS.

To notify, Bretherton and Wyant (1997) suggest that LHF change can lead to a boundary-layer decoupling, which points to less well-mixing. This effect may be in competition with the enhanced mixing from cold advection in some circumstances.

Therefore, apart from the increased local stability, LCC can also directly respond to the upstream Rossby ridge through boundary-layer processes. As deseasonalization has been applied before conducting the composite analyses, the results reflect synoptic perturbations that can occur throughout the year. Table 2 shows that LCC increasing does not rely on EIS increasing. EIS prefers winter circulation, when jets are stronger and synoptic-scale Rossby waves are more active. Meanwhile, LCC shows less seasonal preference, as both the dynamical processes in winter and the larger evaporation in summer (due to warmer SST) favor more LCC.

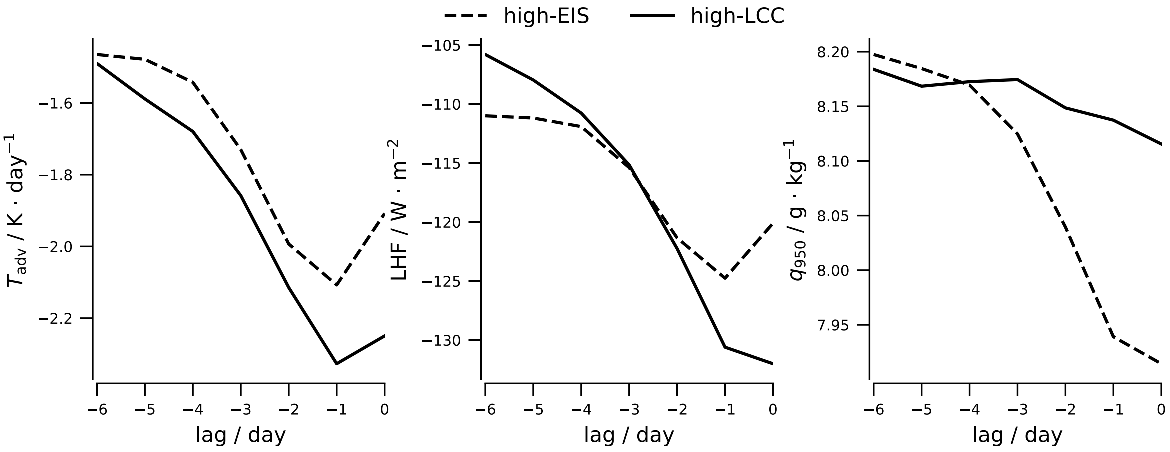

Figure 9. Synoptic evolution of surface temperature advection (T_{adv}, left), surface latent heat flux (LHF, middle), 950 hPa specific humidity (q_{950}, right) in NP composite high-EIS and high-LCC cases. Values are averaged over the Sc area and are normalized by the range of high-EIS cases. Negative values of T_{adv} indicate cold advection, while negative values of LHF indicate an upward surface flux (i.e., evaporation), and vice versa.

Table 2. Seasonal occurrence (in %) of high-EIS and high-LCC cases on synoptic timescales. Values show the fraction of cases occurring in DJF and JJA relative to the total number of cases.

	high-EIS		high-LCC	
	DJF	JJA	DJF	JJA
NP	34	11	32	12
NA	28	17	25	20
SI	13	33	18	28
SP	17	36	24	26
SA	9	40	20	27

5.3 The role of SST on interseasonal and interannual timescales

Unlike the short timescales, when EIS increases due to the column response of the synoptic-scale atmospheric Rossby ridge, the long-term variability of EIS is also influenced by SST.

Although EIS and LCC correlate strongly on long timescales, Figure 10 suggests that it might be due to some shared influence by low-frequency circulations. Comparing the interseasonal patterns (panels b and d), LCC prefers upstream SST warming, while EIS prefers local SST cooling, once the annual cycle is removed. The upstream warming associated with LCC is consistent with De Szoeke et al. (2016). In addition, the discrepancy between LCC and EIS identified on synoptic timescales (i.e., stronger pressure gradients for LCC versus more localized high-pressure anomalies for EIS) remains on interseasonal timescales.

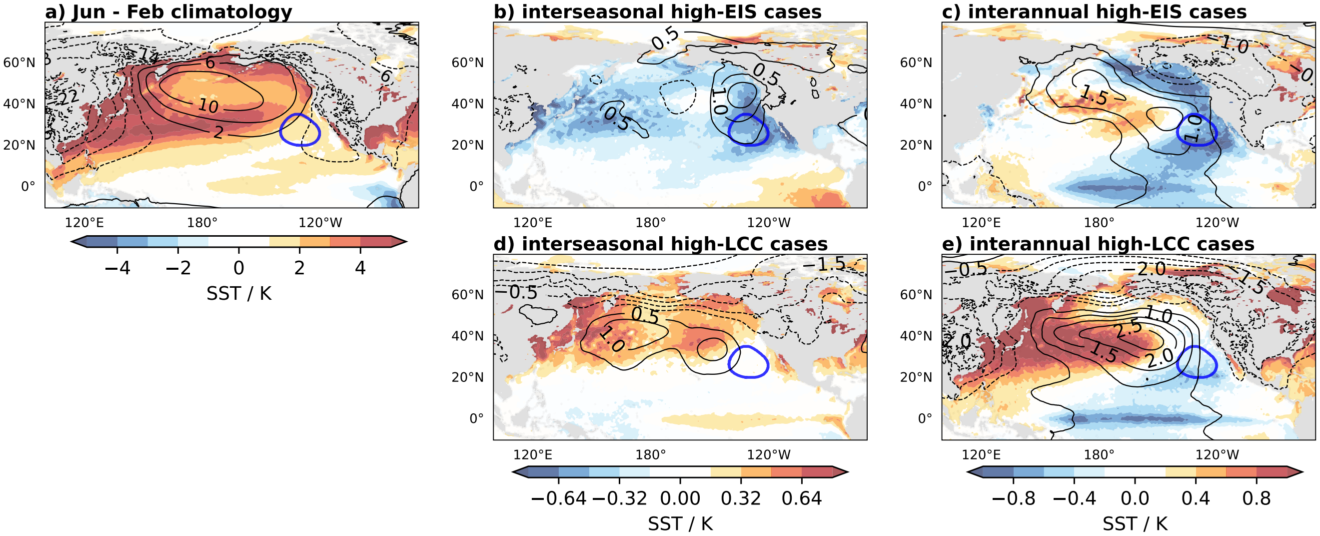

Figure 10. Maps of SST (filled contours) and SLP (contour lines): a) difference between June and February in the climatology; b) anomalies from the climatological mean in the interseasonal high-EIS cases; c) anomalies from the climatological mean in the interannual high-EIS cases; d–e) are similar as b–c) but for the high-LCC cases. (Panels b and d for all regions in Figure S13; panels c and e in Figure S14.)

That discrepancy can be hidden well if including the annual cycle. Figure 10a shows the circulation change from winter to summer. We see that SST shows a -PDO-like pattern, which has a warm tongue upstream with relative cool in the Sc area. This relative cool, together with higher atmospheric pressure in summer, increases EIS. Meanwhile, the upstream warm tongue, coupled with higher pressure upstream, favor more LCC. Therefore, EIS and LCC can both increase through different reasons. The strong correlation (usually >0.8) between EIS and LCC on the annual cycle may be confounded by this set of circulation change.

Similar reason leading to high correlation between EIS and LCC on interannual timescales (panels c and e). On interannual timescales, atmospheric circulation coupled with SST pattern. Negative phase of PDO-like structures co-control EIS and LCC, while the preference of regions still shows. The coupling between this -PDO-like pattern and LCC is also observed in model simulations (Bellomo et al., 2014).

6 Conclusions and discussion

This study establishes the relationships between large-scale circulation and stratocumulus (Sc), and finds that low-cloud cover (LCC) and estimated inversion strength (EIS) respond differently to circulation perturbations.

Instead of the tropical thermodynamic framework, we find an extratropical dynamics control EIS variability. On synoptic and subseasonal timescales, local synoptic-scale Rossby ridges enhance EIS by increasing the stability of the tropospheric column. Due to near-field orography (e.g., the Rocky Mountains, the Andes, and the South African Plateau), these synoptic-scale Rossby ridges can be amplified around Sc areas. This amplification makes synoptic-scale Rossby ridges pronounce on longer timescales, especially in NP, SP, and SA with significant orography. On interseasonal timescales, both atmospheric Rossby ridges and local SSTs influence EIS variability. On interannual timescales, EIS variability is associated with the negative phase of a PDO-like ($-$PDO-like) pattern, in which the atmosphere and ocean circulation are coupled. The $-$PDO-like pattern features extratropical planetary-scale Rossby ridges in the atmosphere and cooler SSTs in the Sc area, both of which can increase EIS. About 76% of EIS variability is explained by the above circulation perturbations, quantified using local 250,hPa geopotential height, 250,hPa vorticity, and SST from 33-year daily series (details of the quantification method are provided in the Supplement, last page).

EIS and LCC exhibit different dependence on similar circulation patterns. Compared with EIS, LCC shows larger dependence on upstream perturbations. Specifically, LCC is associated with upstream Rossby ridges (about a 10° shifted pattern) and upstream SST warming. The reason for this upstream preference is that LCC prefers stronger near-surface winds, which can result from larger pressure gradients. Stronger near-surface winds in the Sc area enhance cold advection and destabilize the marine boundary-layer, thereby enhancing turbulent mixing and favoring more Sc (Klein et al., 1995). Meanwhile, stronger near-surface winds also lead to larger evaporation, which can offset a major part of the drying effect associated with Rossby ridges. Upstream SST warming also supports the enhancement of these boundary-layer processes. Therefore, although EIS tends to prefer winter conditions after deseasonalization, as synoptic-scale Rossby waves are more active in winter, LCC show little seasonal dependence as summer conditions supply more moisture. Solely using EIS explains about 34% of LCC variability, while solely using upstream circulation (quantified using the same method as for EIS variability, but with the averaging region shifted 10° upstream) explains about 36% of LCC variability. Using EIS and upstream circulation together increases the explained variance to 45%, indicating that upstream circulation can direct influence LCC apart from varying EIS. This finding is consistent with Lewis et al. (2023) and Lewis and Bellon (2025), although they interpret the upstream preference as a lagged response to upstream EIS.

The different circulation dependence of EIS and LCC suggests that their strong correlation on long timescales is confounded by the $-$PDO-like circulation structure, which has cooler local SSTs and warmer upstream SSTs that favor both EIS and LCC. We suggest that future studies consider the influence of this pattern when investigating long-term changes in Sc.

The 10° upstream-shifted pattern associated with LCC variability explains why Sc responds to conditions from one day earlier (Klein et al., 1995), as this distance corresponds to about one day of advection at a typical near-surface wind speed in these regions. Therefore, the "one-day-lagged covariance" likely reflects the influence of enhanced near-surface winds on LCC, which are more strongly perturbed by synoptic-scale Rossby waves than by long-term variability in the zonal-mean flow.

Code and data availability. Both ERA5 (Hersbach et al., 2017) and CLARA-A3 dataset (Karlsson et al., 2022) are available at Climate Data Store (https://cds.climate.copernicus.eu/datasets). MODES (Žagar et al., 2015) is available at https://modes.cen.uni-hamburg.de/software.

Author contributions. HD designed and conducted the analyses and wrote the manuscript. BS initiated the research objects and reviewed the manuscript. FL provided systematic input on the analyses and reviewed the manuscript. NŽ initiated and provided support on methodology and reviewed the manuscript. NŽ, BS, and FL contributed suggestions for interpretation.

Competing interests. The authors declare that no competing interests are present.

Acknowledgements. We thank Hauke Schmidt for testing ideas and interpretations. We thank Bernat Jiménez-Esteve for sharing thoughts on the orographic effects. We thank Volkmar Wirth and Tim Woollings for sharing thoughts on the influence of jets. We thank Katharina Holube, Sergiy Vasylkevych, Franziska Glassmeier, Helene Marie Glöckner for their inputs, and Peishan Chen for sharing her experience with the wave decomposition. We thank Divya Sri Praturi for doing internal review. We thank the dataset and supercomputer resources provided by DKRZ (Deutsches Klimarechenzentrum), as well as the Marin cluster supported by CEN-IT (IT services of the Center for Earth System Research and Sustainability) at Universität Hamburg. Generative AI (ChatGPT) was used for grammar checking and language polishing.

References

Bellomo, K., Clement, A., Mauritsen, T., Rädel, G., and Stevens, B.: Simulating the role of subtropical stratocumulus clouds in driving Pacific climate variability, Journal of Climate, 27(13), 5119–5131, https://doi.org/10.1175/JCLI-D-13-00548.1, 2014.

Bretherton, C. and Blossey, P.: Low cloud reduction in a greenhouse-warmed climate: Results from Lagrangian LES of a subtropical marine cloudiness transition, Journal of Advances in Modeling Earth Systems, 6(1), 91–114, https://doi.org/10.1002/2013MS000250, 2014.

Bretherton, C. and Wyant, M.: Moisture transport, lower-tropospheric stability, and decoupling of cloud-topped boundary layers, Journal of the atmospheric sciences, 54(1), 148–167, https://doi.org/10.1175/1520-0469(1997)054<0148:MTLTSA>2.0.CO;2, 1997.

Charney, J. G. and Eliassen, A.: A numerical method for predicting the perturbations of the middle latitude westerlies, Tellus, 1(2), 38–54, https://doi.org/10.3402/tellusa.v1i2.8500, 1949.

Chen, H., Xu, H., Ma, J., and Deng, J.: Why is the mid-tropospheric North Atlantic subtropical high much stronger than the North Pacific subtropical high in boreal summer?, Climate Dynamics, 59(5), 1883–1895, https://doi.org/10.1007/s00382-021-06074-3, 2022.

Chen, P., Hoerling, M., and Dole, R.: The origin of the subtropical anticyclones, Journal of Atmospheric Sciences, 58(13), 1827–1835, https://doi.org/10.1175/1520-0469(2001)058<1827:TOOTSA>2.0.CO;2, 2001.

Chen, P., Holube, K., Lunkeit, F., Žagar, N., Zhao, Y. B., and Lu, R.: Equatorial wave circulation associated with subseasonal convective variability over the subtropical western North Pacific in boreal summer, Weather and Climate Dynamics, 6(4), 1629–1642, https://doi.org/10.5194/wcd-6-1629-2025, 2025.

Cherchi, A., Annamalai, H., Masina, S., and Navarra, A.: South Asian summer monsoon and the eastern Mediterranean climate: The monsoon–desert mechanism in CMIP5 simulations, Journal of Climate, 27(18), 6877–6903, https://doi.org/10.1175/JCLI-D-13-00530.1, 2014.

Cutler, L., Brunke, M., and Zeng, X.: Re-evaluation of low cloud amount relationships with lower-tropospheric stability and estimated inversion strength, Geophysical Research Letters, 136(11), e2022GL098 137, https://doi.org/10.1029/2022GL098137, 2022.

De Szoeke, S., Verlinden, K., Yuter, S., and Mechem, D.: The time scales of variability of marine low clouds, Journal of climate, 29(18), 6463–6481, https://doi.org/10.1175/JCLI-D-15-0460.1, 2016.

Ding, H., Stevens, B., and Schmidt, H.: Factors causing stratocumulus to deviate from subtropical high variability on seasonal to interannual timescales, Atmospheric Chemistry and Physics, 25(18), 10 511–10 521, https://doi.org/10.5194/acp-25-10511-2025, 2025.

Dong, B., Gregory, J., and Sutton, R.: Understanding land–sea warming contrast in response to increasing greenhouse gases. Part I: Transient adjustment, Journal of Climate, 22(11), 3079–3097, https://doi.org/10.1175/2009JCLI2652.1, 2001.

Gaetani, M., Pohl, B., Douville, H., and Fontaine, B.: West African Monsoon influence on the summer Euro-Atlantic circulation, Geophysical Research Letters, 38(9), L09 705, https://doi.org/10.1029/2011GL047150, 2011.

Garfinkel, C., White, I., Gerber, E., Adam, O., and Jucker, M.: Nonlinear interaction between the drivers of the monsoon and summertime stationary waves, Geophysical Research Letters, 48(14), e2020GL092 321, https://doi.org/10.1029/2020GL092321, 2021.

George, R. and Wood, R.: Subseasonal variability of low cloud radiative properties over the southeast Pacific Ocean, Atmospheric Chemistry and Physics, 10(8), 4047–4063, https://doi.org/10.5194/acp-10-4047-2010, 2010.

Hartmann, D., Ockert-Bell, M.E., and Michelsen, M.: The effect of cloud type on Earth's energy balance: Global analysis, Journal of Climate, 5, 1281–1304, https://doi.org/10.1175/1520-0442(1992)005<1281:TEOCTO>2.0.CO;2, 1992.

Hersbach, H., Bell, B., Berrisford, P., Hirahara, S., Horányi, A., Muñoz-Sabater, J., Nicolas, J., Peubey, C., Radu, R., Schepers, D., Simmons, A., Soci, C., Abdalla, S., Abellan, X., Balsamo, G., Bechtold, P., Biavati, G., Bidlot, J., Bonavita, M., De Chiara, G., Dahlgren, P., Dee, D., Diamantakis, M., Dragani, R., Flemming, J., Forbes, R., Fuentes, M., Geer, A., Haimberger, L., Healy, S., Hogan, R., Hólm, E., Janisková, M., Keeley, S., Laloyaux, P., Lopez, P., Lupu, C., Radnoti, G., de Rosnay, P., Rozum, I., Vamborg, F., Villaume, S., and Thépaut, J.-N.: Complete ERA5 from 1940: Fifth generation of ECMWF atmospheric reanalyses of the global climate [dataset], Copernicus Climate Change Service (C3S) Data Store (CDS), Data distribution by the German Climate Computing Center (DKRZ). 10.24381/cds.143582cf (accessed on 2023-06-15), 2017.

Hoskins, B. and Ambrizzi, T.: Rossby wave propagation on a realistic longitudinally varying flow, Journal of Atmospheric Sciences, 50(12), 1661–1671, https://doi.org/10.1175/1520-0469(1993)050<1661:RWPOAR>2.0.CO;2, 1993.

Hoskins, B. and Karoly, D.: The steady linear response of a spherical atmosphere to thermal and orographic forcing, Journal of Atmospheric Sciences, 38(6), 1179–1196, https://doi.org/10.1175/1520-0469(1981)038<1179:TSLROA>2.0.CO;2, 1981.

Hotz, B., Papritz, L., and Röthlisberger, M.: Understanding the vertical temperature structure of recent record-shattering heatwaves, Weather and Climate Dynamics, 5(1), 323–343, https://doi.org/10.5194/wcd-5-323-2024, 2024.

Jiménez-Esteve, B., Kornhuber, K., and Domeisen, D. I. V.: Heat extremes driven by amplification of phase-locked circumglobal waves forced by topography in an idealized atmospheric model, Geophysical Research Letters, 49(21), e2021GL096 337, https://doi.org/10.1029/2021GL096337, 2022.

Karlsson, K.-G., Stengel, M., Meirink, J. F., Riihelä, A., Trentmann, J., Akkermans, T., Stein, D., Devasthale, A., Eliasson, S., Johansson, E., Håkansson, N., Solodovnik, I., Benas, N., Clerbaux, N., Selbach, N., Schröder, M., and Hollmann, R.: CLARA-A3: The third edition of the AVHRR-based CM SAF climate data record on clouds, radiation and surface albedo covering the period 1979 to 2023 [dataset], Copernicus Climate Change Service (C3S) Climate Data Store (CDS). 10.24381/cds.68653055 (accessed on 2025-07-01), 2022.

Kasahara, A.: Normal modes of ultralong waves in the atmosphere, Mon. Wea. Rev., 104, 669–690, 1976.

Klein, S. A.: Synoptic variability of low-cloud properties and meteorological parameters in the subtropical trade wind boundary layer, Journal of Climate, 10(8), 2018–2039, https://doi.org/10.1175/1520-0442(1997)010<2018:SVOLCP>2.0.CO;2, 1997.

Klein, S. A. and Hartmann, D. L.: The Seasonal Cycle of Low Stratiform Clouds, Journal of Climate, 6(8), 1587–1606, https://doi.org/10.1175/1520-0442(1993)006<1587:TSCOLS>2.0.CO;2, 1993.

Klein, S. A., Hartmann, D. L., and Norris, J. R.: On the relationships among low-cloud structure, sea surface temperature, and atmospheric circulation in the summertime northeast Pacific, Journal of Climate, 8(5), 1140–1155, https://doi.org/10.1175/1520-0442(1995)008<1140:OTRALC>2.0.CO;2, 1995.

Lawrence, M. G.: The relationship between relative humidity and the dewpoint temperature in moist air: A simple conversion and applications, Bulletin of the American Meteorological Society, 86(2), 225–234, https://doi.org/10.1175/BAMS-86-2-225, 2005.

Lewis, H. and Bellon, G.: Systematic upstream large-scale control of subtropical low-cloud properties, Journal of Climate, 38(1), 327–346, https://doi.org/10.1175/JCLI-D-24-0181.1, 2025.

Lewis, H., Bellon, G., and Dinh, T.: Upstream large-scale control of subtropical low-cloud climatology, Journal of Climate, 36(10), 3289–3303, https://doi.org/10.1175/JCLI-D-22-0676.1, 2023.

Liu, X., Grise, K., Schmidt, D., and Davis, R.: Regional characteristics of variability in the Northern Hemisphere wintertime polar front jet and subtropical jet in observations and CMIP6 models, Journal of Geophysical Research: Atmospheres, 126(22), e2021JD034 876, https://doi.org/10.1029/2021JD034876, 2021.

Myers, T. and Norris, J.: Observational evidence that enhanced subsidence reduces subtropical marine boundary layer cloudiness, Journal of climate, 26(19), 7507–7524, https://doi.org/10.1175/JCLI-D-12-00736.1, 2013.

Neduhal, V., Žagar, N., Lunkeit, F., Polichtchouk, I., and Zaplotnik, Ž.: Decomposition of the horizontal wind divergence associated with the Rossby, mixed Rossby-gravity, inertia-gravity, and kelvin waves on the sphere, Journal of Geophysical Research: Atmospheres, 129(9), e2023JD040 427, https://doi.org/10.1029/2023JD040427, 2024.

Nigam, S. and Chan, S.: On the summertime strengthening of the Northern Hemisphere Pacific sea level pressure anticyclone, Journal of climate, 22(5), 1174–1192, https://doi.org/10.1175/2008JCLI2322.1, 2009.

Park, S. and Shin, J.: Heuristic estimation of low-level cloud fraction over the globe based on a decoupling parameterization, Atmospheric Chemistry and Physics, 19(8), 5635–5660, https://doi.org/10.5194/acp-19-5635-2019, 2019.

Polster, C. and Wirth, V.: A new atmospheric background state to diagnose local waveguidability, Geophysical Research Letters, 50(24), e2023GL106 166, https://doi.org/10.1029/2023GL106166, 2023.

Rodwell, M. and Hoskins, B.: Subtropical anticyclones and summer monsoons, Journal of Climate, 14(15), 3192–3211, https://doi.org/10.1175/1520-0442(2001)014<3192:SAASM>2.0.CO;2, 2001.

Rodwell, M. J. and Hoskins, B. J.: Monsoons and the dynamics of deserts, Quarterly Journal of the Royal Meteorological Society, 122(534), 1385–1404, https://doi.org/10.1002/qj.49712253408, 1996.

Sardeshmukh, P. and Hoskins, B.: The generation of global rotational flow by steady idealized tropical divergence, Journal of Atmospheric Sciences, 45(7), 1228–1251, https://doi.org/10.1175/1520-0469(1988)045<1228:TGOGRF>2.0.CO;2, 1988.

Schubert, W., Ciesielski, P., Lu, C., and Johnson, R.: Dynamical adjustment of the trade wind inversion layer, Journal of Atmospheric Sciences, 52(16), 2941–2952, https://doi.org/10.1175/1520-0469(1995)052<2941:DAOTTW>2.0.CO;2, 1995.

Scott, R., Myers, T., Norris, J., Zelinka, M., Klein, S., Sun, M., and Doelling, D.: Observed sensitivity of low-cloud radiative effects to meteorological perturbations over the global oceans, Journal of Climate, 33(18), 7717–7734, https://doi.org/10.1175/JCLI-D-19-1028.1, 2020.

Siebesma, A., Jakob, C., Lenderink, G., Neggers, R., Teixeira, J., Van Meijgaard, E., Calvo, J., Chlond, A., Grenier, H., Jones, C., Köhler, M., Kitagawa, H., Marquet, P., Lock, A., Müller, F., Olmeda, D., and Severijns, C.: Cloud representation in general-circulation models over the northern Pacific Ocean: A EUROCS intercomparison study, Quarterly Journal of the Royal Meteorological Society, 130(604), 3245–3267, https://doi.org/10.1256/qj.03.146, 2004.

Stephens, G.: Cloud feedbacks in the climate system: A critical review, Journal of Climate, 18(2), 237–273, https://doi.org/10.1175/JCLI-3243.1, 2005.

Stevens, B., Ackerman, A., Albrecht, B., Brown, A., Chlond, A., Cuxart, J. ., and Stevens, D.: Simulations of trade wind cumuli under a strong inversion, Journal of the Atmospheric Sciences, 58(14), 1870–1891, https://doi.org/10.1175/1520-0469(2001)058<1870:SOTWCU>2.0.CO;2, 2001.

Takaya, K. and Nakamura, H.: A Formulation of a Phase-Independent Wave-Activity Flux for Stationary and Migratory Quasi-geostrophic Eddies on a Zonally Varying Basic Flow, Journal of the Atmospheric Sciences, 58, 608–627, https://doi.org/10.1175/1520-0469(2001)058<0608:AFOAPI>2.0.CO;2, 2001.

Toniazzo, T., Abel, S., Wood, R., Mechoso, C., Allen, G., and Shaffrey, L.: Large-scale and synoptic meteorology in the south-east Pacific during the observations campaign VOCALS-REx in austral Spring 2008, Atmospheric Chemistry and Physics, 11, 4977–5009, https://doi.org/10.5194/acp-11-4977-2011, 2011.

Wirth, V.: Waveguidability of idealized midlatitude jets and the limitations of ray tracing theory, Weather and Climate Dynamics, 1(1), 111–125, https://doi.org/10.5194/wcd-1-111-2020, 2020.

Wood, R.: Stratocumulus clouds, Monthly weather review, 140(8), 2373–2423, https://doi.org/10.1175/MWR-D-11-00121.1, 2012.

Wood, R. and Bretherton, C.: Boundary layer depth, entrainment, and decoupling in the cloud-capped subtropical and tropical marine boundary layer, Journal of Climate, 17(18), 3576–3588, https://doi.org/10.1175/1520-0442(2004)017<3576:BLDEAD>2.0.CO;2, 2004.

Wood, R. and Bretherton, C.: On the relationship between stratiform low cloud cover and lower-tropospheric stability, Journal of Climate, 19(24), 6425–6432, https://doi.org/10.1175/JCLI3988.1, 2006.

Žagar, N., Neduhal, V., Vasylkevych, S., Ž. Zaplotnik, and Tanaka, H.: Decomposition of vertical velocity and its zonal wavenumber kinetic energy spectra in the hydrostatic atmosphere, J. Atmos. Sci., 80, 2747–2767, https://doi.org/10.1175/JAS-D-23-0090.1, 2023.

Zhang, Y., Li, J., Hou, Z., Zuo, B., Xu, Y., Tang, X., and Wang, H.: Climatic effects of the Indian Ocean tripole on the Western United States in boreal summer, Journal of Climate, 35(8), 2503–2523, https://doi.org/10.1175/JCLI-D-21-0490.1, 2022.

Zilli, M. and Hart, N.: Rossby wave dynamics over South America explored with automatic tropical–extratropical cloud band identification framework, Journal of Climate, 34(20), 8125–8144, https://doi.org/10.1175/JCLI-D-21-0020.1, 2021.

Žagar, N. and Franzke, C. L.: Systematic decomposition of the Madden-Julian Oscillation into balanced and inertio-gravity components, Geophysical Research Letters, 42(16), 6829–6835, https://doi.org/10.1002/2015GL065130, 2015.

Žagar, N., Kasahara, A., Terasaki, K., Tribbia, J., and Tanaka, H.: Normal-mode function representation of global 3-D data sets: Open-access software for the atmospheric research community, Geoscientific Model Development, 8(4), 1169–1195, https://doi.org/10.5194/gmd-8-1169-2015, 2015.